Supplementary Information

High-power wearable triboelectric nanogenerator prepared from self-assembled electrospun poly(vinylidene fluoride) fibers with heart-like structure

Jia-Han Zhang,[ab] Yong Li,[a] Jinhua Du,[a] Xihong Hao,*[ab] and Haitao Huang[c]

[a] *Inner Mongolia Key Laboratory of Ferroelectric-related New Energy Materials and Devices, Inner Mongolia University of Science and Technology, Baotou 014010, China.*

[b] *Key Laboratory of Integrated Exploitation of Bayan Obo Multi-Metal Resources, Inner Mongolia University of Science and Technology, Baotou 014010, China*

[c] *Department of Applied Physics, The Hong Kong Polytechnic University, Hung Hom, Kowloon, Hong Kong, China*

E-mail: xhhao@imust.cn (X. Hao)

* Corresponding Author.

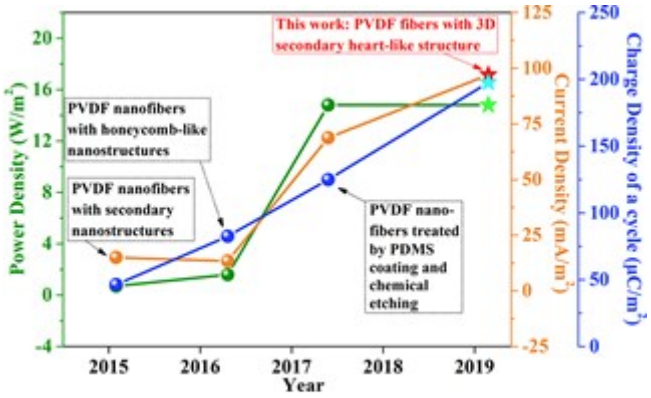

Fig. S1. The power densities, current densities and charge densities of various electrospun PVDF fiber based TENGs reported in the past few years.

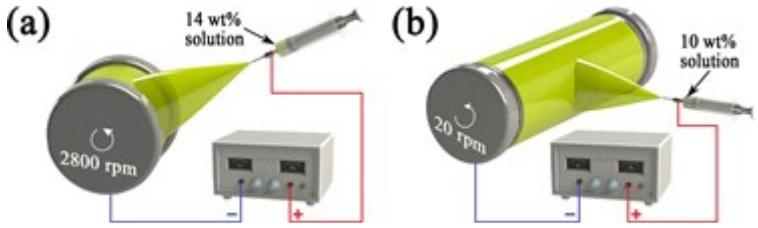

Fig. S2. Schematic diagrams of the electrospinning setups for preparing (a) the 2D primary nanofiber mat and (b) the 3D primary micro-nanofiber mat.

The apparatus consists of a syringe with a needle connected to a high positive voltage DC power supply and a drum collect connected to a high negative voltage DC power supply. Under the Coulombic repulsive force within the jet and the electrostatic force, the droplet at the needle tip forms a Taylor cone. When the Coulombic force overcomes the surface tension of PVDF solution, an electrified jet is ejected from the needle tip and deposits onto the drum collector. During this process, the solvent gradually evaporates. It is known that the surface tension and the Coulombic repulsive force are the driving forces for reducing the surface area of the liquid and promoting extension of the jet, respectively. Comparing with a 14 wt% PVDF solution, the 10 wt% solution is less viscous and its solvent is more difficult to be evaporated completely. Therefore, the effect of the surface tension on the droplet whose concentration is 10 wt% is

more significant. Similarly, the influence of the Coulombic repulsive force on the droplet whose concentration is 14 wt% is more remarkable. As a consequence, the 2D primary nanofibers and the 3D primary micro-nanofibers are obtained by controlling the concentrations of PVDF solution being 14 wt% and 10 wt%, respectively.

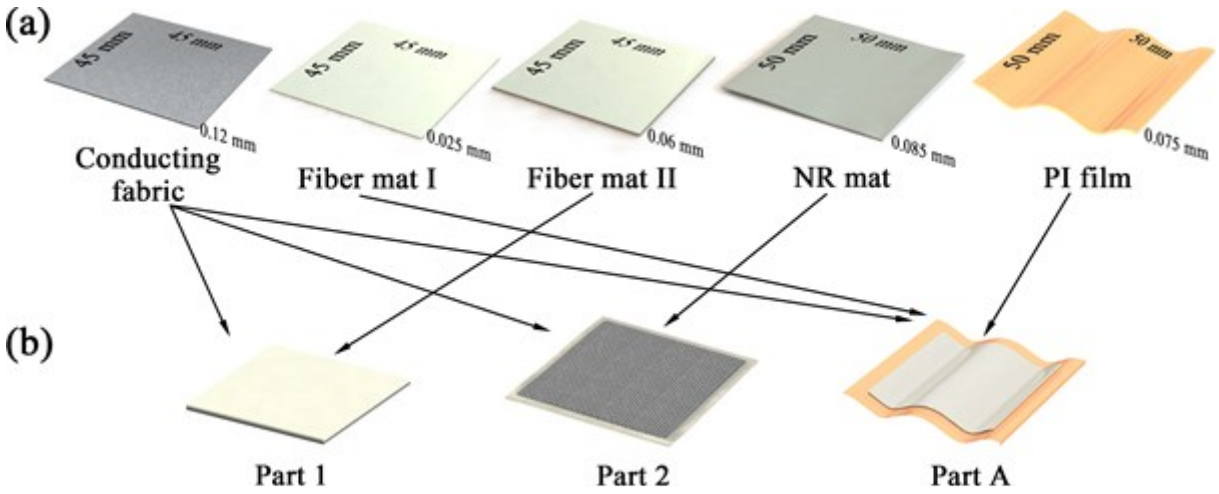

Fig. S3. Schematic diagram of (a) the components and (b) the assemblies of the TENG.

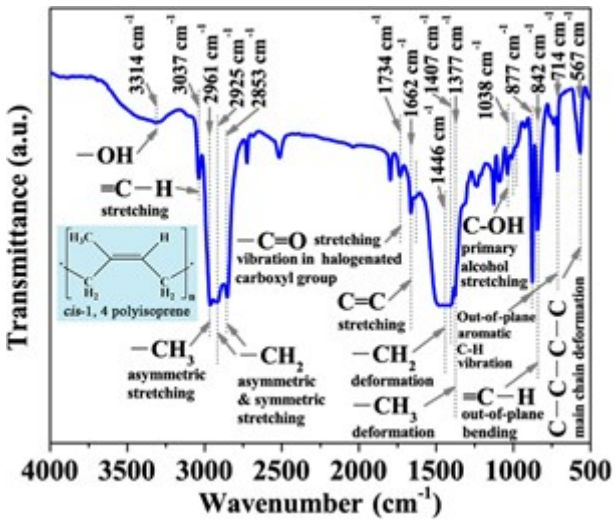

Fig. S4. FT-IR spectrum of the NR mat. The inset shows the structural formula of the main constituent, *cis*-1, 4 polyisoprene, of NR.

Table S1. Peak wavenumbers and assignations for the NR mat.

Peak wavenumber cm^{-1}	Assignation	Ref.
3314	−OH	1,2
3037	=C−H stretching	1
2961	$-CH_3$ asymmetric stretching	1
2925	$-CH_2$ asymmetric stretching	1
2853	$-CH_2$ symmetric stretching	2
1407	−CH2 scissoring vibration of R−S−S−CH_2−R′ and/or R−S−CH_2−R′	3
1734	−C=O stretching vibration in halogenated carboxyl group	4
1662	C=C stretching	1
1637	Carbonyl C=O	5
1446	$-CH_2$ deformation	1
1377	C−H bending vibrations of $-CH_3$ in propylene unit	6
1038	C−OH primary alcohol stretching	1
1008	Out of plane bending vibrations of =C−H of vinyl groups	6,7
979	−C−H vibrations of butadiene double bond	7-9
877 & 714	Out-of-plane aromatic C−H vibration	4
842	=C−H out-of-plane bending	1
567	C−C−C−C natural rubber main chain deformation	1

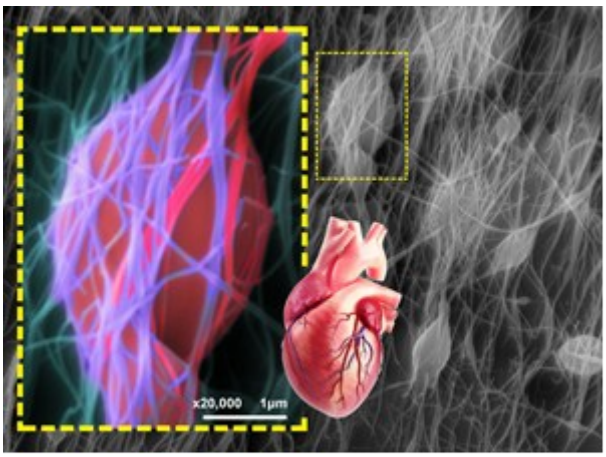

Fig. S5. SEM image of the 3D secondary heart-like fiber mat. Insets show the magnified colored SEM image of the area encircled by a yellow dotted line and the schematic illustration of a human heart. According to above two insets, the 3D secondary PVDF fiber possesses a heart-like structure. The spindle-shaped microsphere looks like the main part of a heart, and a lot of thin nanowires wrapping around the microsphere, just like cardiac arteries and cardiac veins.

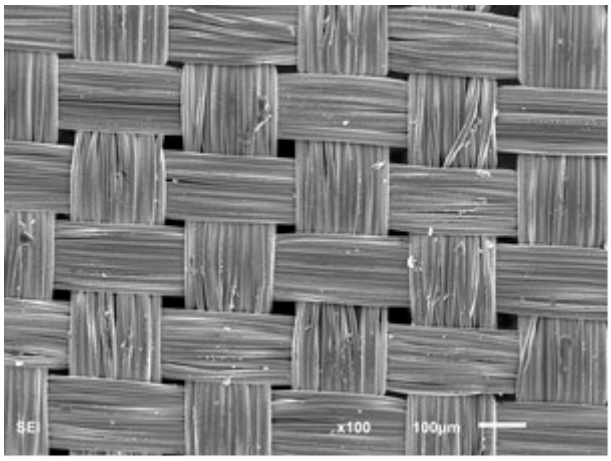

Fig. S6. SEM image of the conducting fabric.

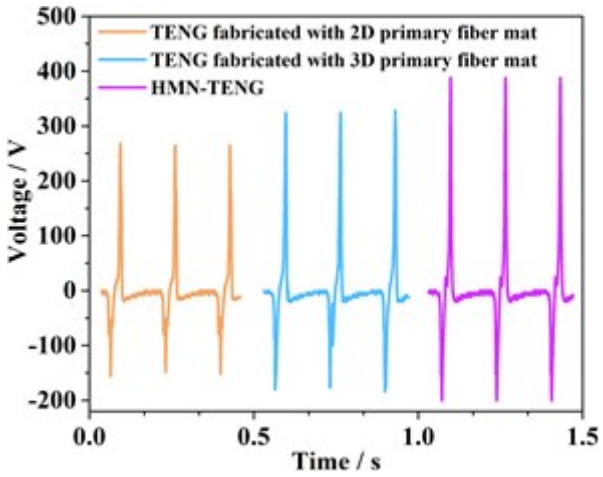

Fig. S7. The output voltages of the TENG fabricated with 2D primary fiber mat, the TENG fabricated with 3D primary fiber mat, and the HMN-TENG measured by the custom-made apparatus with the constant force of 5.8 N.

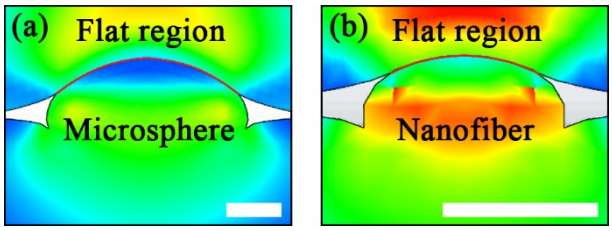

Fig. S8. The deformed condition of (a) the microsphere and (b) the nanofiber under the same pressure according to ABAQUS simulation. Scale bar: 500 nm. The red curves represent the contact surface.

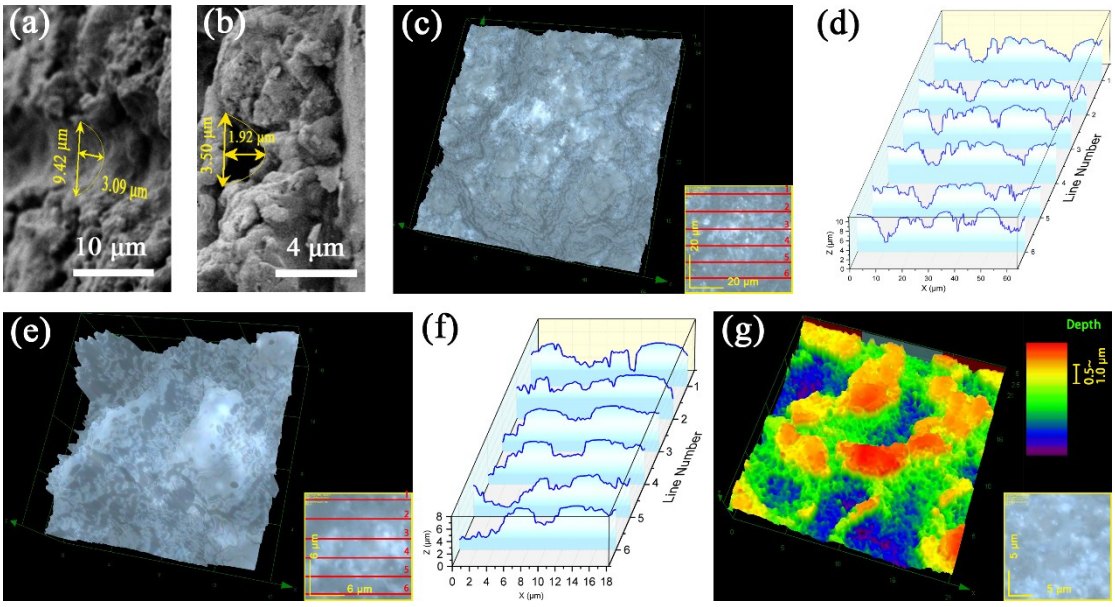

Fig. S9. SEM images of (a) the ravine-like structures and (b) the porous structures on the NR mat. (c) 3D surface morphology of the NR mat. (d) Vertical distance-horizontal distance curves of the NR mat as presented in the inset of Fig. S9c. (e) Magnified 3D surface morphology of the NR mat. (f) Vertical distance-horizontal distance curves of the NR mat as presented in the inset of Fig. S9e. (g) Colored 3D surface morphology of the NR mat. The insets show optical microscope photographs of corresponding test areas, and the red lines represent the regions for obtaining vertical distance-horizontal distance curves.

As shown in Fig. S9a and S9b, it has been demonstrated that the surface of NR mat consists of three different microstructures, namely the flat, the porous and the ravine-like structures. The 3D surface morphology and the vertical distance-horizontal distance curves in Fig. S9c−S9g show a same result, and some regular conclusions can be drawn. The depressed porous and ravine-like structures with bigger diameters possess greater depths. According to the SEM image in Fig. $3b_1$ and the vertical distance-horizontal distance curves in Fig. S9d and S9f, the diameters of the porous structures are limited between 0.7 and 3.5 μm, and their average size is 2.2 μm. Meanwhile, the diameters of the ravine-like structures are limited between 3.5 and 18.0 μm, and their average size is 6.2 μm. There exists relationship between the diameter and the

depth of above depressed structures. The diameter to depth ratios for porous structures and ravine-like structures are around 2:1 and 3:1, respectively. The average ratio of diameter to depth for porous structures and ravine-like structures are 2.1 and 3.3, respectively, which are obtained via Fig. S9d and S9f. It should be noted that Fig. S9e and S9f are only representative pictures, more pictures were used to calculate the average ratio of diameter to depth for porous structures to guarantee accuracy. Fig. S9g shows the colored 3D surface morphology of the NR mat. Different color represents different depth. Red and orange represent flat surface; yellow, green, blue and purple represent depressed structures. The NR mat has irregular pores and ravine-like structures, whereas all of the irregular structures are depressed. Meanwhile, a part of depressed structures are not deep. After calculated via an image processing software (Adobe Photoshop CC 2017), the proportion for flat red and orange regions is 34.1%. The yellow region with shallow depth (approximately 0.5−1.0 μm) occupies 20.6% of total area, and the green region with medium depth (approximately 1.0−2.0 μm) occupies 32.9% of total area. The proportion for blue and purple regions with great depth (approximately 2.0−5.3 μm) is 12.4%. Accordingly, when two friction layers are in contact with each other, the 3D secondary heart-like fiber mat can fill the vacant spaces of shallow depressed structures (approximately 0.5−1.0 μm) due to the relatively irregular spindle structures with a diameter range of 0.70−3.77 μm and an average diameter of 1.8 μm. The deeper structures probably also be filled owing to the high elasticity of NR mats. In contrast, the relatively regular 2D primary nanofibers with large length-diameter ratio have less opportunity to fill the vacant spaces.

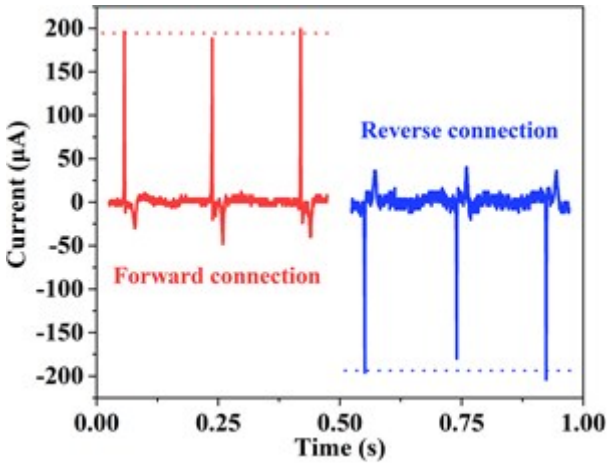

Fig. S10. Measured currents under the forward and the reverse connection modes, respectively.

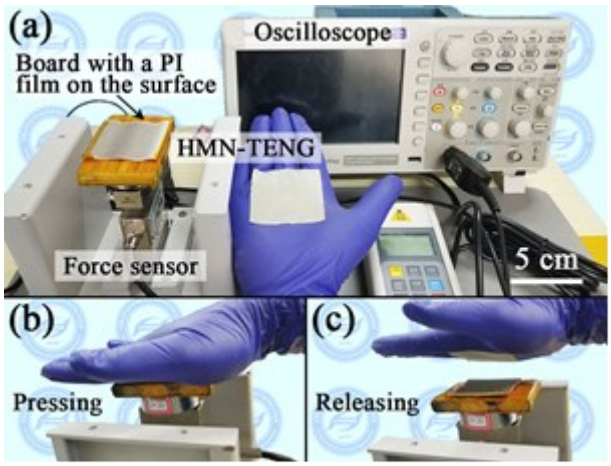

Fig. S11. Photographs of (a) the test setup platform, (b) pressing state and (c) releasing state during hand patting. In the experiment, a PI film was pasted on the surface of the board for the sake of reducing electrostatic charge generated between the top surface of the board and the bottom surface of Part A of the HMN-TENG.

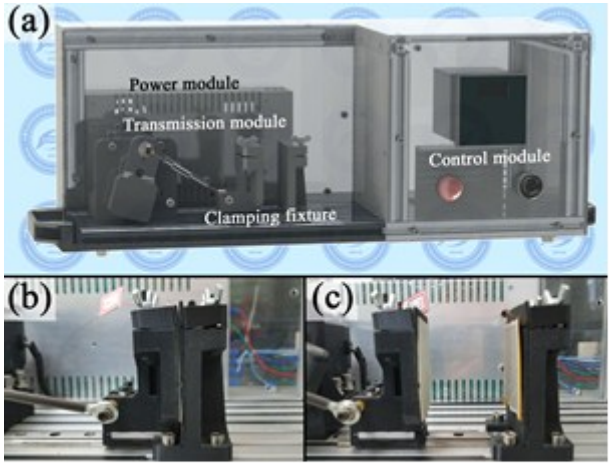

Fig. S12. (a) Schematic diagram of the custom-made apparatus for testing piezoelectric and triboelectric properties. Photographs of (b) pressing state and (c) releasing state when the HMN-TENG was tested.

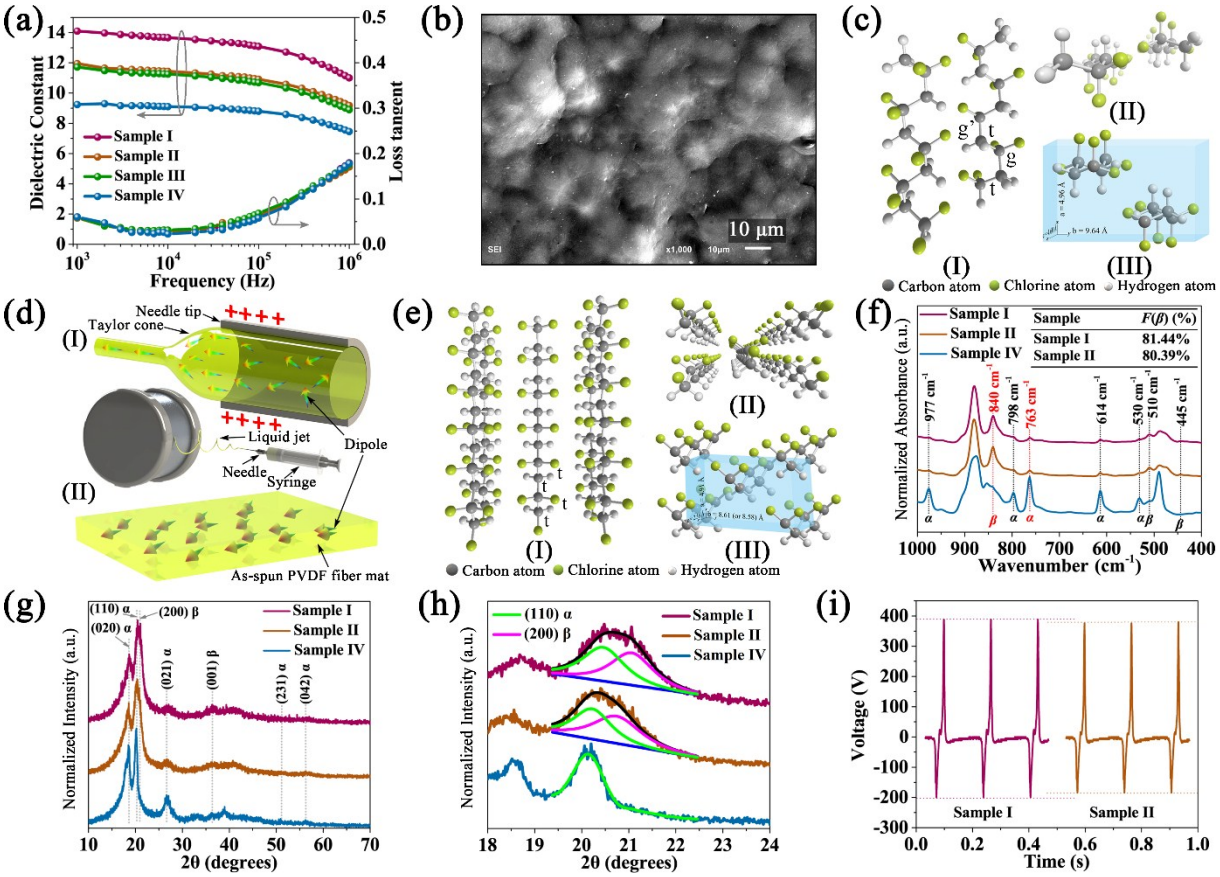

Fig. S13. (a) Frequency dependence of dielectric constant values and loss tangent for Sample I-Sample IV. (b) The SEM image of Sample IV. The spherulites in the SEM image are of the antipolar *α* phase. (c) Schematic depictions of (I) polymer chain segments in *trans-gauche* conformation (*tgtg′*), (II) *α* chain conformation in PVDF, and (III) the unit cell of *α phase.* (d) Schematic illustration of arrangement of the dipoles (I) in the needle tip and (II) in the as-spun PVDF fiber mat. (e) Schematic depictions of (I) polymer chain segments in all *trans* planar zigzag conformation (*tttt*), (II) *β* chain conformation in PVDF, and (III) the unit cell of *β* phase. (f) FT-IR spectra of Sample I, Sample II and Sample IV. The inset table shows *β* phase contents of Sample I and Sample II. (g) XRD patterns of Sample I, Sample II and Sample IV. (h) Expanded view of the second peak in (g) and their curve deconvolution. (i) The output voltages of Sample I and Sample II measured by the custom-made apparatus with the constant force of 5.8 N.

Note S1: The detailed explanation on advantage of electrospinning in improving dielectric constant

Electrospinning is a promising technique to improve the polarizability of PVDF due to three forces acting on the PVDF solution.[10] As plotted in Fig. S13d-I, a shear force firstly acts on the solution when it flows through a capillary needle. Subsequently, a coulombic force elongates the jet. Finally, a mechanical force applied by a drum collector with high rotating speed stretches the fiber. All of the forces can cause molecular chains to be stretched and aligned, and promote the generation of β phase whose conformer is longer *all-trans* planar zigzag conformation (*tttt*) (Fig. S13e). Another typical phase in PVDF is α phase with shorter *trans-gauche* conformation (*tgtg′*) (Fig. S13c). In the *all-trans* conformation of β phase, the CF dipoles are perpendicular to the chain axis, causing the repeat unit with a high dipole moment of 7.0×10^{-30} C m.[11] In contrast, for the lowest energy conformer, α phase, the dipole moment of its repeat unit is nil because of the antiparallel chain packing.[12-14] Accordingly, β-PVDF possesses higher dielectric constant than α-PVDF. Correspondly, the pristine 3D secondary heart-like electrospun PVDF fiber mat (Sample I) should have high dielectric constant. For comparison, the mat experiencing annealing at 80 °C for 15 h (Sample II), the mat experiencing annealing at 80 °C for 30 h (Sample III), and the mat remolded from melt cooling (Sample IV) were also prepared, and their dielectric constants, FT-IR spectra and XRD patterns were performed. It is necessary to note that annealing at 80 °C cannot damage the surface morphologies of the samples. As shown in Fig. S13a, the lowest dielectric constant was observed in Sample IV, which was 35% below that of Sample I whose dielectric constant was highest. This is because Sample IV contains a large amount of α phase, which can be demonstrated by characteristic spherulite structure of α phase in Fig. S13b and representative absorption bands and peaks assigned to α phase. As shown in Fig. S13f, for Sample IV, the FT-IR absorption bands at 977, 798, 763, 614 and 530 cm^{-1} assigned to α phase were sharp and obvious,[15-17] whereas absorption bands of β phase including 840 and 510 cm^{-1} were extremely

weak.[15,16] XRD patterns showed the same trend (Fig. S13g). Two representative peaks of β phase at 20.8° and 36.4° correspond to the (200) plane and the (100) plane, respectively.[15,16] The rest of peaks at 18.6°, 20.2°, 26.7°, 51.2° and 56.3° are attributed to the diffraction in (020), (110), (021), (231) and (042) planes of the α phase, respectively.[15,16] To clearly distinguish two peaks at 20.2° and 20.8°, deconvolution was conducted, and the result is given in Fig. 11h. The peak intensity of β (200) for Sample IV almost disappeared, whereas the peak intensity of α (110) was significantly high. On the contrary, for Sample I, the representative absorption bands and peaks of β phase were very sharp, but those of α phase were very weak. It is therefore concluded that electrospinning is conducive to improving dielectric constant by boosting the formation of β phase.

Note S2: The detailed description on a small contribution from the ruduction of β phase content during temperature aging to the decrease of dielectric constant

As shown in Fig. S13a, Compared with Sample I, the sample after temperature aging for 15 h had distinctly lower dielectric constant, and as the annealing time was prolonged from 15 to 30 h, the dielectric constants barely changed. According to a previous report,[18] undergoing temperature aging, the aligned dipoles in β-PVDF will reorientate and become disoriented. This may be the major reason for the decrease of dielectric constant. Meanwhile, we observed the area of the sample after temperature aging was reduced by about 5.0%. Consequently, we guess that longer *all-trans* planar zigzag conformation (*tttt*) may convert to shorter *trans-gauche* conformation (*tgtg′*) during temperature aging process even though the annealing temperature is below the Curie temperature. In order to prove the above-mentioned guess, the β phase fractions, $F(\beta)$, in the complete crystalline phases of Sample I and Sample II were calculated using the following **Equation S1**:[12,15,16,19]

$$F(\beta) = \frac{A_\beta}{1.26A_\alpha + A_\beta} \tag{S1}$$

in which A_α and A_β represent the absorbance intensities at 763 and 840 cm^{-1}, respectively. After temperature aging, the fraction of β phase decreased from 81.44% to 80.39% (Fig. S13f), which proves the fact that temperature aging can lead to the slight decrease of β phase content, which may be associated with sample shrinking during annealing process.

Note S3: The detailed description on the generation of macroscopic polarization during electrospinning process

After electrospinning, the mat possessed aligned dipoles, leading to weak macroscopic polarization perpendicular to the mat surface. As diagrammed in Fig. S13d-I, it is probably because when the electrified jet has just ejected from the needle tip, their dipoles are aligned along the fiber direction.[11,12] After a moment, the straight jet undergoes whipping and then deposits onto the collector,[12,20,21] which means the jet direction is not parallel to electric field direction during whipping process, leading to reorientation of dipoles and generation of weak macroscopic polarization perpendicular to the mat surface. Although the electrospun PVDF mat possesses macroscopic polarization perpendicular to the mat surface, the direction of dipoles is may not completely perpendicular to the mat surface. There may exists only perpendicular component (Fig. S13a-II).

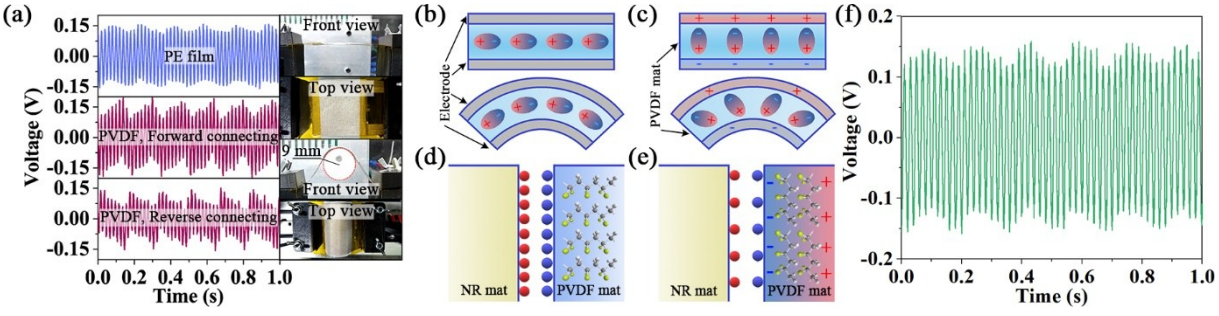

Fig. S14. (a) The output voltages of the piezoelectric nanogenerators assembled using PE film and Sample I. Insets show the top views and the front views corresponding to straightened and bent piezoelectric nanogenerator, respectively. Schematic illustrations of (b) the indistinctive change of piezoelectrically induced charges, comparing the releasing state with the bending state, (c) the distinctive change of piezoelectrically induced charges, comparing the releasing state with the bending state, (d) significant charge transfer occurred between the rubber film and the electrospun PVDF fiber mat because dipoles were arranged parallel to the top and the bottom surfaces of the PVDF mat, and (e) less charge transfer occurred between the rubber film and the PVDF mat when aligned dipoles were not completely perpendicular to the top and the bottom surfaces of the PVDF mat. (f) The output voltages of the piezoelectric nanogenerators assembled using Sample II.

Note S4: The evidence related to the existence of macroscopic polarization perpendicular to the mat surface after electrospinning and the analysis about the negative effect of the macroscopic polarization

Fig. S14a shows output piezoelectric signals of Sample I, which is tested with the frequency of 6 Hz and the bending radius of 9.0 mm, and authenticity was proved *via* a forward and a reverse connection measurements. The output voltage was 0.036 V as compared with a polyethylene (PE) film with the same size and under the same testing conditions. It is noted that the PE film has no piezoelectricity. The existence of piezoelectric signals indicates that there is macroscopic polarization perpendicular to the mat surface. This is because when the dipoles are all parallel to the mat surface and no macroscopic polarization exists along the direction perpendicular to the mat surface, the assembled piezoelectric nanogenerator barely has electric output signal (Fig. S14b). In contrast, when the direction of aligned dipoles is not parallel to the mat surface, macroscopic polarization perpendicular to the mat surface will be detected. Moreover, equal

and opposite induced charges exist in a pair of electrodes, which endows the assembled piezoelectric nanogenerator with piezoelectric signals (Fig. S14c).

In addition, based on the electric field direction in electrospinning, one end of dipole with negative charge is closer to the upper surface of the mat compared with another end of dipole with positive charge (Fig. S14e). Here, the upper surface of the PVDF fiber mat is the surface which is in contact with the tribopositive layer. Therefore, the existence of macroscopic polarization weakens the ability of the mat to trap negative charges (Fig. S14d and S14e).

Note S5: The evidence related to the disappearance of macroscopic polarization after temperature aging

According to above analysis, since temperature aging disorientates the aligned dipoles in *β*-PVDF, the treated PVDF fiber mat no longer possessed macroscopic polarization and piezoelectricity. Therefore, the assembled piezoelectric nanogenerator would have no electric output signal. As shown in Fig. S14f, the test result was consistent with the above prediction.

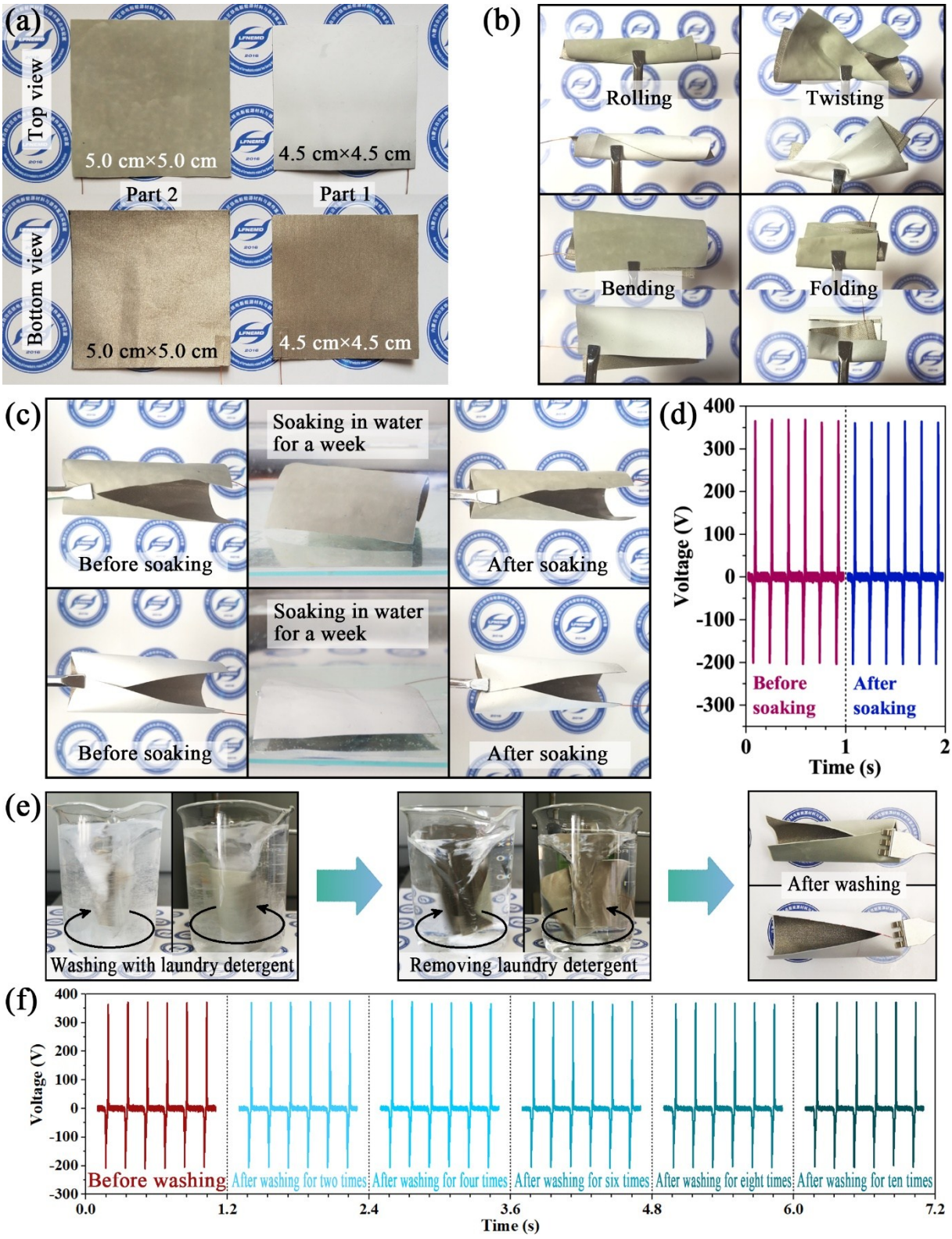

Fig. S15. Photographs of (a) top views and bottom views of Part 1 and Part 2, (b) the states of rolling, twisting, folding and bending. (c–f) Demonstration of washability of the HMN-TENG. (c) Photographs of the soaking process. (d) Output voltages measured before and after soaking for a week *via* the custom-made apparatus with the constant force of 5.8 N. (e) Photographs of

the washing process. (f) Output voltages measured before and after washing via the custom-made apparatus with the constant force of 5.8 N.

As show in Fig. S15e, we washed Part 1 and Part 2 under machine-washing conditions. A complete washing process is as follows. Firstly, Part 1 and Part 2 are washed by using a mixture of water and laundry detergent [product number: 80000662, Bluemoon (China) Co., Ltd.] at room temperature for 20 min. The concentration of laundry detergent is determined as 1 g L^{-1} according to the product description. The time interval between clockwise rotation and counterclockwise rotation is 10 s. Secondly, after rinsing, Part 1 and Part 2 are washed by using water for 10 min. To remove the laundry detergent completely, this step is operated for twice. Finally, Part 1 and Part 2 are aired at room temperature. As presented in Fig. S15f, after the complete washing process was carried out for ten times, there was no layering and no voltage deterioration.

Video S1. Showing 595 blue LEDs were directly lighten up, while subjecting the HMN-TENG to continuous patting motion at the frequency of around 6 Hz.

References

1. M. Valera-Zaragoza, A. Yescas-Yescas, E. A. Juarez-Arellano, A. Aguirre-Cruz, A. Aparicio-Saguilan, E. Ramirez-Vargas, S. Sepulveda-Guzman and S. Sanchez-Valdes, *Polym. Bull.*, 2014, **71**, 1295–1313.

2. T. Kan, V. Strezov and T. Evans, *Fuel*, 2017, **191**, 403–410.

3. X. Y. Chen, S. Q. Zhang, X. L. Wang, X. J. Yao, J. K. Chen, C. W. Zhou, *J. Appl. Polym. Sci.* 1995, **58**, 1401.

4. A. M. Fernandez, C. Barriocanal and R. Alvarez, *J. Hazard. Mater.*, 2012, **203**, 236–243.

5. K. Muniandy, H. Ismail and N. Othman, *Bioresources*, 2012, **7**, 957–971.

6. S. Gunasekaran, R. K. Natarajan and A. Kala, *Spectrochim. Acta A*, 2007, **68**, 323–330.

7. M. J. Fernandez-Berridi, N. Gonzalez, A. Mugica and C. Bernicot, *Thermochim. Acta*, 2006, **444**, 65–70.

8. K. A. Dubkov, S. V. Semikolenov, D. P. Ivanov, D. E. Babushkin and V. D. Voronchikhin, *Iran. Polym. J.*, 2014, **23**, 881–890.

9. S. Chakraborty, S. Bandyopadhyay, R. Ameta, R. Mukhopadhyay and A. S. Deuri, *Polym. Test.*, 2007, **26**, 38–41.

10. C. Wan and C. R. Bowen, *J. Mater. Chem. A*, 2017, **5**, 3091–3128.

11. A. J. Lovinger, *Science*, 1983, **220**, 1115–1121.

12. C. Wan and C. R. Bowen, *J. Mater. Chem. A*, 2017, **5**, 3091–3128.

13. Q. Li and Q. Wang, *Macromolecul. Chem. Phys.*, 2016, **217**, 1228–1244.

14. M. Bohlen and K. Bolton, *Phys. Chem. Chem. Phys.*, 2014, **16**, 12929–12939.

15. B. Mohammadi, A. A. Yousefi and S. M. Bellah, *Polym. Test.*, 2007, **26**, 42–50.

16. N. Jia, Q. He, J. Sun, G. Xia and R. Song, *Polym. Test.*, 2017, **57**, 302–306.

17. M. Li, H. J. Wondergem, M.-J. Spijkman, K. Asadi, I. Katsouras, P. W. M. Blom and D. M. de Leeuw, *Nat. Mater.*, 2013, **12**, 433–438.

18. M. Neidhofer, F. Beaume, L. Ibos, A. Bernes and C. Lacabanne, *Polymer*, 2004, **45**, 1679–1688.

19. J. Fang, H. Niu, H. Wang, X. Wang and T. Lin, *Energ. Environ. Sci.*, 2013, **6**, 2196–2202.

20. Z. M. Huang, Y. Z. Zhang, M. Kotaki and S. Ramakrishna, *Compos. Sci. Technol.*, 2003, **63**, 2223–2253.

21. N. Duc-Nam, Y. Hwang and W. Moon, *European. Polym. J.*, 2016, **77**, 54–64.